Synergetic Interaction of Additive Dual Nanocatalysts to Accelerate Oxygen Reduction Reaction in Fuel Cell Cathodes

Yun Chen,[†] Liang Liang,[†] Sergio A. Paredes Navia,[†] Alec Hinerman,[†] Kirk Gerdes,[‡] and Xueyan Song*,[†] [iD]

[†]Department of Mechanical and Aerospace Engineering, West Virginia University, Morgantown, West Virginia 26506, United States
[‡]National Energy Technology Laboratory, United States Department of Energy, Morgantown, West Virginia 26507, United States

[S] *Supporting Information*

ABSTRACT: The sluggish oxygen reduction reaction (ORR) in the cathode is hindering the power density of solid oxide fuel cells (SOFCs). Infiltration of catalyst into the cathode of SOFCs is promising to accelerate the ORR. However, the degradation associated with the coarsening of the nanocatalyst is intense. To stabilize the catalyst, atomic layer deposition (ALD) is employed to coat a dual electrocatalyst consisting of a superjacent 2 nm CoO_x layer and superjacent 3 nm discrete Pt particles into the porous lanthanum strontium manganite (LSM)/yttria-stabilized zirconia (YSZ) cathode. After 504 h of operation at 750 °C, the ALD coating resulted in the peak power density enhancement by ∼200%, while CoO_x becomes Mn-enriched $(MnCo)O_x$ nanograins coupling with nano-Pt. The $Pt/(MnCo)O_x$ nanocouplings are uniformly distributed on the YSZ grain surface, triple-phase boundaries, and at LSM/LSM surface grain boundaries. This study demonstrates an effective approach of stabilizing the minute amount of catalyst for enhancing ORR activity at elevated temperatures.

KEYWORDS: solid oxide fuel cell, cathode, atomic layer deposition, nanocatalyst, coating, cobalt oxide, platinum, oxygen reduction reaction
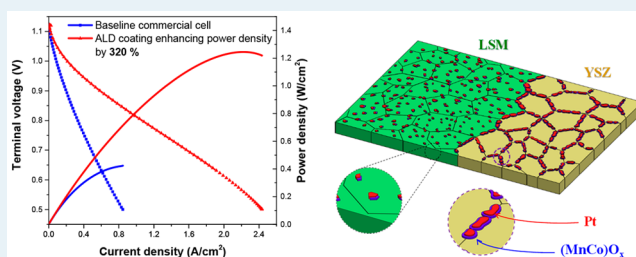
1. INTRODUCTION

In comparison with the emerging protonic ceramic fuel cells,[1−3] the solid oxide fuel cells (SOFCs)[4−7] are these days commercially available with applications including stationary power supply and advanced hybrid fuel cell and engine systems that have the potential of achieving ultrahigh efficiency of greater than 70%.[8,9] Nevertheless, there is an urgent need for further improvement of the SOFC performance in terms of power density and long-term stability to increase their market competencies. The typical power density of a yttria-stabilized zirconia (YSZ)-based commercial SOFC is currently reported to be in the range of ∼0.2−0.8 W/cm^2 depending on the cell configuration (either electrolyte-supported or anode-supported), cathode materials, and the cell operating conditions.[10−13] Regardless of the intense research effort during the past decade, the high activation energy for oxygen reduction reaction (ORR) in the cathode is still the major cause hindering the power density of the state-of-the-art SOFCs. Infiltration processes have thus been developed for deposition of nanoscale catalysts into the well-developed porous lanthanum strontium manganite (LSM) or lanthanum strontium cobalt ferrite (LSCF) based composite cathodes, to enhance the surface electrocatalytic activity and stability and accelerate the ORR.[14−16]

Among the various electrocatalysts, precious metal Pt remains one of the most efficient oxygen reduction catalysts

employed for various fuel cells operated at different temperatures, while the high cost of Pt prevents its large-scale applications. In recent years, chemical vapor based atomic layer deposition (ALD)[17−22] is demonstrated to be able to create a conformal and uniform surface coating layer with thickness down to the atomic scale. Such an approach could lead to the minimum loading of catalyst into the cathode of as-fabricated cells to further improve the SOFC performance.[23] For example, when the ALD layer is ∼5 nm in thickness and consists of discrete ∼3 nm Pt grains, the loading of Pt is estimated to be minute, ∼1.5 × 10^{-3} mg/cm^2, which is significantly lower than the target loading of <0.1 mg/cm^2 that needs to be achieved for proton-exchange membrane fuel cells[24] in automotive applications.[25] However, for SOFC operated at high temperatures of 750 °C or higher, once the ALD monolayer of unary Pt is applied to the LSM/YSZ cathode of cells, the power density enhancement induced by ALD coating is limited to be ∼140%.[23] Pt in the ALD layer undergoes immediate agglomeration from ∼3 to ∼70 nm in dimensions and loss of catalytic surface area due to the electrochemical operation.[23] Pinning the Pt catalyst to be nanosized and with uniform distribution on the ORR active
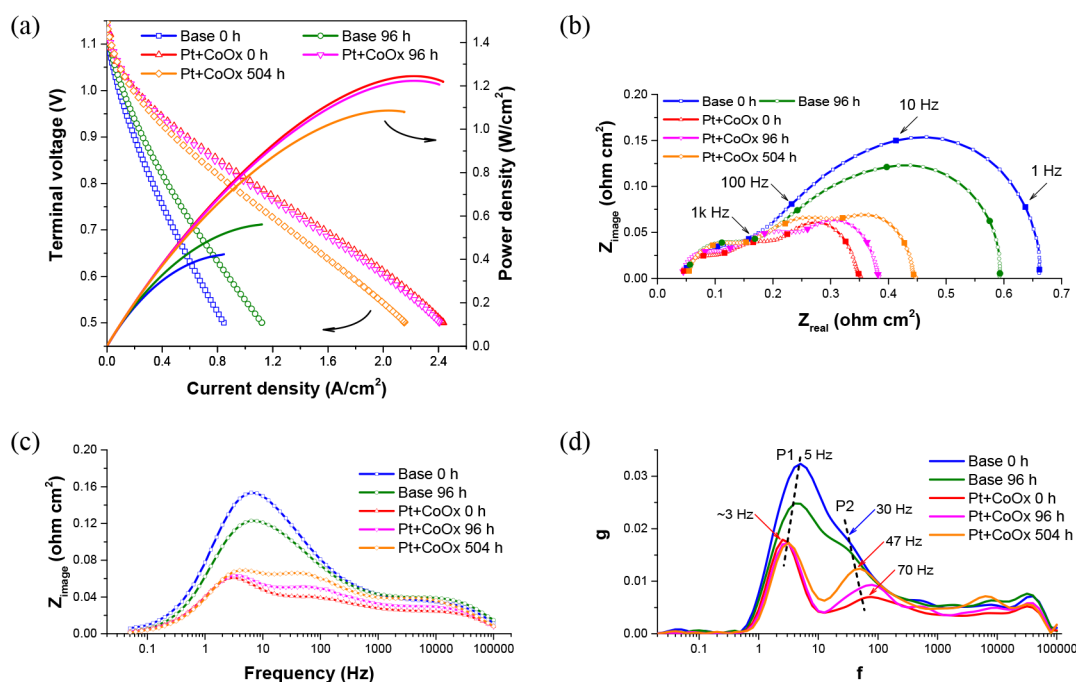
Figure 1. Power density and impedance for cell no. 1 LSM baseline cell and cell no. 2 LSM cell with 3 nm discrete Pt particles capped with a 2 nm Co_3O_4 layer. (a) Terminal voltage as a function of current density for the cells at 750 °C. (b) Nyquist plots of four cells at a constant current of 0.3 A/cm². (c) Bode plots of cells at a constant current density of 0.3 A/cm². (d) Corresponding deconvolution spectra of the impedance data collected from two cells. Two major arcs with the frequency ranging at 1−5 Hz and 10−200 Hz are indicated by P_1 and P_2, respectively.

sites is very much desired to further boost the cell performance while minimizing the Pt loading in the ALD layer. Here we report one simple approach of applying an ultrathin CoO_x layer to stabilize the nano-Pt particles on the LSM/YSZ cathode backbone of as-made SOFCs. Among the various transition metal oxides, CoO_x is selected as the ALD coating layer in the present study because CoO_x is considered to be another promising ORR catalyst in addition to Pt.[26−28] Through synergetic electrochemical interactions, the Pt/ $(MnCo)O_x$ couplings were established and uniformly distributed on the entire YSZ surface, the original triple-phase boundaries (TPBs), and at LSM/LSM surface grain boundaries. Such nanoscale Pt/$(MnCo)O_x$ couplings are stable and dramatically accelerate the ORR. ALD coating has significantly enhanced the cell peak power density by 200% over electrochemical operation of 504 h at 750 °C. For the first time in the field of SOFCs, the present work demonstrated the establishment of minute amount, but stable, nanocatalyst induced by ALD coating and resultant large cell performance enhancement over extended electrochemical operations at elevated temperatures.

2. EXPERIMENTAL SECTION

Commercially available, anode-supported solid oxide button cells fabricated by Materials and Systems Research, Incorporated (MSRI, Salt Lake City, UT) were employed for all the experiments described in this paper. MSRI cells are composed of five layers as follows, starting from the anode: ∼0.9 mm thick Ni/YSZ cermet layer which supports the cell structure, 15 μm thick Ni/YSZ active layer, ∼12 μm thick YSZ electrolyte, ∼15 μm thick $La_{0.8}Sr_{0.2}MnO_3$/8YSZ active layer, and 50 μm thick, pure LSM current collecting layer. The cell active area (limited by the cathode) is 2 cm². The exposure area of the anode to fuel is about 3.5 cm².

The ALD coatings were performed in a commercial GEMStar-8 ALD reactor from Arradiance Inc. The precursors used in this study were all purchased from Strem Chemicals, Inc. The (trimethyl)methylcyclopentadienylplatinum(IV) (99%) and the deionized water were used as Pt precursor and oxidant for depositing the Pt layer, and the bis-(cyclopentadienyl)cobalt(II) (min 98% cobaltocene) and ozone were used as Co and oxidant, respectively, for CoO_x layer growth. During the deposition, the (trimethyl)-methylcyclopentadienylplatinum and bis(cyclopentadienyl)-cobalt containers were maintained at 75 and 90 °C, respectively, and the reactor chamber was set at 300 °C. A total 50 cycles were performed for each element deposition, leading to a dual-layer ALD coating of ∼3 nm Pt first, followed by 2 nm of Co_3O_4, as schematically shown in Figure S1. This is simply one-step processing of as-received cells, and the change of the chemistry in the ALD layer was achieved through computer-controlled automatic switching of the precursors. No masking or specific treatment is applied on the NiO/YSZ anode of the as-received cells before ALD processing. In practice, the thick and very dense NiO/YSZ anode prevents precursor penetration during the ALD processing, and the impact of ALD coating on the Ni/YSZ anode is negligible. No surface pretreatment was applied to the cells, and no heat treatment was applied before or after ALD coating either. The cell electrochemical operation was carried out directly after the ALD coating.

Totally, two cells including one baseline cell (cell no. 1) and one with the ALD dual coating layer (cell no. 2) were examined. Both cell tests were performed on a test stand. The platinum mesh was used for anode and cathode lead connections. The fuel and air stream flow rates were controlled separately using mass flow controllers. Cell testing was performed at 750 °C. During the operation, a 600 mL/min

Table 1. Power Density and Resistance of the Baseline Cell No. 1 and the ALD-Coated Cell No. 2

cell no.	time (h)	R_s (Ω cm^2)	R_p (Ω cm^2)	peak power (W/cm^2)	power at 0.8 V (W/cm^2)	enhancement of power density at 0.8 V
1	0	0.034	0.660	0.420	0.266	
1	96	0.037	0.586	0.556	0.357	
2	0	0.041	0.309	1.245	0.863	3.2 (to cell no. 1 at 0 h)
2	96	0.040	0.345	1.224	0.826	2.3 (to cell no. 1 at 96 h)
2	504	0.050	0.399	1.090	0.725	2.0 (to cell no. 1 at 96 h)

air flow rate and a 600 mL/min fuel flow rate were used. Before any electrochemical measurements, both cells were current-treated for approximately ~15 h under a small current density of 0.1 A/cm^2 to ensure they were activated. After that, the samples were loaded at a constant current of 0.3 A/cm^2 for desired periods. The cell performance was examined using a TrueData-Load modular electronic dc load which guarantees voltage and current accuracies of 0.03% FS of the range selected ±0.05% of value. The cell impedance spectra were examined using a potentiostat/galvanostat (Solartron 1287A) equipped with a frequency response analyzer (Solartron 1260). Impedance measurements were carried out using a Solartron 1260 frequency response analyzer in a frequency range from 50 mHz to 100 kHz. The impedance spectra and resistance (R_s and R_p) presented are those measured under a dc bias current of 0.3 A/cm^2. On a Nyquist plot, R_s is determined by the intercept at the higher frequency end, and R_p is determined by the distance between two intercepts.

After electrochemical operation, the ALD-coated cell was sectioned and subjected to nanostructural and crystallographic examination using high-resolution (HR) transmission electron microscopy (TEM). All the TEM examinations were conducted in the cathode active layer. TEM samples were prepared by mechanical polishing and ion milling in a liquid-nitrogen-cooled holder. Electron diffraction, diffraction contrast, and HRTEM imaging were performed using a JEM-2100 operated at 200 kV. Chemical analysis was carried out under TEM using energy-dispersive X-ray spectroscopy (EDS).

3. RESULTS AND DISCUSSION

3.1. Performance Enhancement Induced by ALD Coating.
Upon the electrochemical operation at 750 °C, baseline cell no. 1 experienced the activation process,[29] with increased power density (Figure 1a and Table 1) during initial operation. From 0 to 96 h of operation, cell no. 1 shows a slight increase of the ohmic resistance R_s, but a decrease of the polarization resistance R_p, as depicted in the Nyquist and Bode plots in Figure 1, parts b and c. The baseline cell no. 1 possess a peak power density of 0.556 W/cm^2 after the operation at 0.3 A/cm^2 for 96 h. By contrast, at 0 h of operation, cell no. 2 shows the immediate higher peak power density of 1.245 W/cm^2, that is a 320% enhancement in comparison to that of the baseline. The power density increase is accompanied by the large reduction of R_p by 52%. Further cell operation resulted in a slight increase of R_p in cell no. 2. After being operated at 0.3 A/cm^2 for 504 h, the peak density of cell no. 2 is 1.09 W/cm^2, which remains ~200% over that of cell no. 1 operated for 96 h. To the best of our knowledge, this is so far the highest performance enhancement for state-of-the-art commercial cells that is achieved using various impregnation techniques.[30−37] Due to the negligible amount of ALD materials coated onto the internal surface of the porous cathode of the as-fabricated cells, the ~200% increase is simultaneously achieved in terms of both power density and specific power.

To identify the physical origin of cell performance enhancement and resistance reduction, the dynamic constant in the impedance data is retrieved by evaluating the relaxation times and relaxation amplitude of the impedance-related processes using deconvolution shown in Figure 1d.[38−42] In cell no. 1, two arcs are present in the frequency range between 0.6 and 200 Hz, while arc P_1 contributed the highest proportion of resistance and arc P_2 is exhibited as a shoulder projecting from P_1. By contrast, cell no. 2 presented two distinct peaks of P_1 and P_2 that are both significantly lower than that from cell no. 1. Over 504 h of operation, the amplitude of the P_1 in cell no. 2 has little change, while the P_2 continually increases with the operation. Meanwhile, the P_2 arcs in cell no. 2 continuously shift to the lower frequency end with the increase of operation duration. On the basis of the impedance deconvolution, the subsequent equivalent circuit fitting and the capacitance analysis were performed on both cells, as detailed in the Supporting Information and Figures S2−S6. There is increased chemical capacitance[43,44] revealing the possible involvement of the cathode bulk in the overall electrode reaction in the ALD-coated cell (discussed in the Supporting Information).

3.2. Strongly Coupled Pt/(MnCo)O$_x$ Pairs on the Cathode Surface.
The above deconvolution analysis reveals that the ORR kinetics have been significantly altered in cell no. 2 induced by ALD coating. For SOFC, the ORR and oxygen ion transport kinetics are largely affected by the nanostructure of electrode-active surfaces that are directly interacting with the reactant gas species. The nanostructure and chemistry from the cathode internal surface of the ALD-coated cell no. 2 are thus subjected to TEM imaging and analysis.

In cell no. 2 with 504 h of operation, Pt particles with the size of ~50 nm were found to populate at LSM/YSZ/air interfaces or the original TPB regions shown in Figure 2a. The formation of Pt particles at TPBs is consistent with our previous study.[23] The as-deposited ALD Pt nanoparticles with ~3 nm in dimension may have been oxidized and vaporized as Pt−O gas species (dominant in PtO$_2$) when the cell is heated to high temperatures in air. However, upon electrochemical operation under current load, oxygen partial pressure is sharply reduced locally at TPBs. PtO$_2$ is thus subsequently reduced to metallic Pt and reassembled preferentially at the electrochemically reactive sites of TPBs, where the oxygen partial pressure is the lowest on the cathode internal surface.[45] In the cell with unary Pt ALD coating, the Pt redeposition is merely taking place at the TPBs, and both the YSZ and the LSM surfaces are free of Pt nanograins.[23,46] However, once the dual catalysts Pt and Co are applied using ALD, much smaller Pt particles of ~10 nm in thickness uniformly and densely distributed on all YSZ grain surface in cell no. 2, as shown in Figure 2, parts b and c. Some of the Pt possesses a well-defined crystal orientation relationship with the YSZ backbone, implying reassembly of Pt on the YSZ surface. Meanwhile, the Pt nanograins remain to be a metallic single phase as confirmed
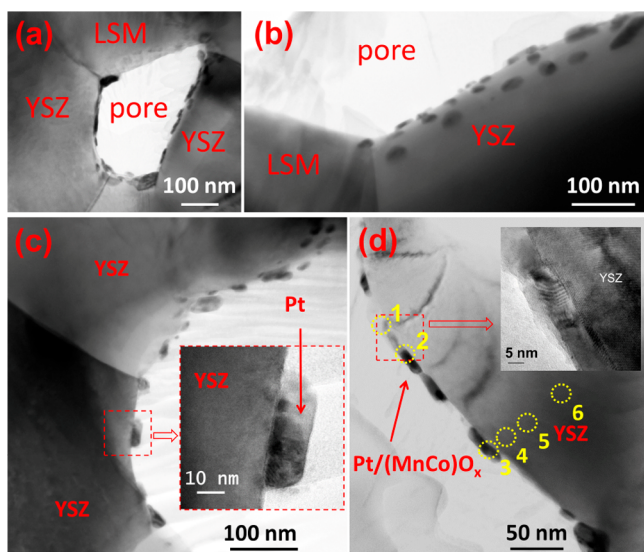
Figure 2. Representative TEM images from cell no. 2 LSM cell after 504 h of operation. (a) Bimodel distribution of the particles with the bigger particles exclusively at the original TPBs. (b) Small Pt and $(MnCo)O_x$ grains are on the YSZ surface, and the LSM grain is free of secondary-phase grains. (c) Small and discrete Pt and $(MnCo)O_x$ particles on the YSZ surface. (d) Overlapping $(MnCo)O_x$ and Pt grains on the YSZ surface. Local EDS examination was conducted for those numbered spots (in yellow dashed circles), and the results are listed in Table 2. The size of the circles indicates approximate beam size being used for EDS spectrum collection. EDS points 1−3 indicate the chemistry of $Pt/(MnCo)O_x$ coupling on the YSZ surface. EDS points 4−6 indicate that the YSZ grains are free of Co and with a minor and fixed Mn amount.

by electron diffraction pattern shown in Figure S7. Furthermore, Pt grains are found not to solely exist on the YSZ surface. Next to the Pt, there are always coupling elongated $(MnCo)O_x$ nanograins. In the TEM images, along the electron beam imaging direction, the $(MnCo)O_x$ nanograins are largely overlapping with Pt grains (shown in the inset of Figure 2d). The $(MnCo)O_x$ grains are also about ∼10 nm in thickness and appear to be with various Mn/Co ratios,

but always Mn-enriched according to the EDS (in Figure 2 and Table 2).

Underneath the ALD layer, the YSZ grains do not present detectable Co signals, implying Co does not dope YSZ at all. Nevertheless, the backbone YSZ grains were alloying with a minor amount of Mn and La, with a fixed level of ∼3% of Mn/ (Zr + Mn + Y + La). Cations Mn and La in YSZ are believed to migrate from the neighboring LSM, and Mn saturates in the YSZ during the cathode fabrication processing.[47] Since only CoO_x and Pt were deposited using ALD, the formation of Mn-enriched $(MnCo)O_x$ grains is apparently caused by the Mn−Co cation exchanges. Such cation exchange is presumably along the YSZ surface because Co is not alloying with YSZ and Mn saturated with limited solubility in YSZ.

In cell no. 2, different from the YSZ surfaces that were decorated by the dense $Pt/(MnCo)O_x$ nanocouplings, in the regions that are away from the TPBs and grain boundaries, the LSM grain surface is free of nanoparticles (shown in Figure 2, parts a and b). Interestingly, besides the YSZ surface, the $Pt/(MnCo)O_x$ couplings are also populating along the LSM/LSM surface grain boundaries, as depicted in Figure 3a. The cross-sectional view images of Figure 3, parts b and c, show that the Pt at LSM/LSM grain boundary region is striplike and elongated for about ∼50 nm along the LSM grain surface. Coupling the striplike Pt, Co appears to concentrate locally at the LSM surface grain boundary region as well (shown in Figure 3 and Table 2). Directly underneath the $Pt/(MnCo)O_x$ coupling, LSM grains are with a constant level of 2% of Co/ (Co + Mn), that is the same as the LSM grain interior. Away from the grain boundary/air interface, there is no Mn or Co enrichment on the LSM grain surface.

According to the nanostructure analysis, the distribution of stable Pt−Co dual catalysts in cell no. 2 after extended operation for 504 h at 750 °C is schematized in Figure 4. The $Pt/(MnCo)O_x$ coupling are densely and uniformly distributed on the YSZ surface, populated at the original TPBs, and dispersed at LSM/LSM surface grain boundaries.

3.3. Synergetic Interaction of Dual Catalysts and Evidence of the Ionic Conductivity from Co-Doped LSM Surface Grain Boundaries. As mentioned previously, ALD

Table 2. Chemistry Analyzed Using EDS from the Selected Points in the Figures

| EDS spot no.	atomic %								normalized formula
	O	La	Sr	Mn	Co	Zr	Y	Pt	
1	31.90			56.50	0.29	5.49		5.83	
2	33.04			53.46	0.64	2.45		10.40	
3	15.56			5.81	1.26	7.52		69.85	
4	44.32	1.06		2.41		44.22	7.99		$(Y_{0.14}Mn_{0.04}La_{0.02}Zr_{0.79})O_x$
5	49.87	0.87		2.21		39.66	7.39		$(Y_{0.15}Mn_{0.04}La_{0.02}Zr_{0.79})O_x$
6	57.40	0.65		1.64		33.99	6.32		$(Y_{0.15}Mn_{0.04}La_{0.02}Zr_{0.80})O_x$
7	69.11	11.80	2.70	16.19	0.20				$(La_{0.81}Sr_{0.19})_{0.9}(Mn_{0.99}Co_{0.01})O_x$
8	73.27	8.07	1.83	15.25	0.36			1.22	$(La_{0.82}Sr_{0.18})_{0.63}(Mn_{0.98}Co_{0.02})O_x + Pt$
9	70.45	9.00	1.92	12.67	0.44	1.15		4.36	$(La_{0.82}Sr_{0.18})_{0.83}(Mn_{0.97}Co_{0.03})O_x + Pt + Zr$
10	64.03	13.43	3.19	18.87	0.48				$(La_{0.81}Sr_{0.19})_{0.86}(Mn_{0.98}Co_{0.02})O_x$
11	65.39	13.15	2.97	17.87	0.63				$(La_{0.82}Sr_{0.18})_{0.87}(Mn_{0.97}Co_{0.03})O_x$
12	67.37	11.98	2.99	17.21	0.45				$(La_{0.80}Sr_{0.20})_{0.85}(Mn_{0.97}Co_{0.03})O_x$
13	63.21	10.53		23.37				2.89	
14	44.53	4.94		16.95	2.85			30.73	
15	56.12	6.17	1.16	17.43	1.64			17.47	
16	64.89	9.26	2.23	16.60	0.86			6.16	$(La_{0.81}Sr_{0.19})_{0.66}(Mn_{0.95}Co_{0.05})O_x + Pt$
17	69.35	11.45	2.42	16.10	0.22	0.47			$(La_{0.83}Sr_{0.17})_{0.85}(Mn_{0.99}Co_{0.01})O_x$
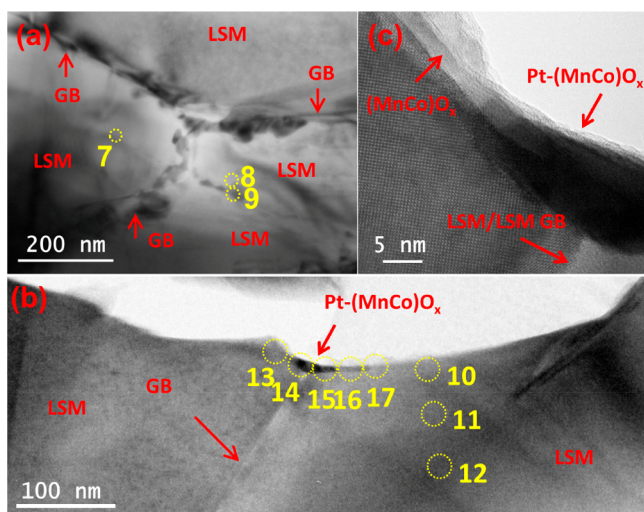
Figure 3. Representative TEM images from cell no. 2 LSM cell after 504 h of operation. (a) The surface of the LSM grain boundaries is decorated with the nanoparticles. EDS points 7−9 in Table 2 demonstrate that the Pt is only present at the LSM/LSM surface grain boundaries. (b) Cross section of the LSM grain boundary with the secondary particles sitting at the LSM/LSM grain boundaries. EDS points 13−16 (in Table 2) indicate that the striplike Pt is coupled by Co enrichment. Away from the surface grain boundaries regions, the LSM surface is without Pt (EDS points 10 and 17), and there is little variation of Co concentration from the LSM grain surface to the grain interior (EDS points 10−12). (c) Showing the enlarged portion of the $(MnCo)O_x$ grains and the adjacent Pt nanograins of panel b.

coating of unary ∼3 nm Pt particles experienced the acute Pt agglomeration to >70 nm and reassembled at TPBs immediately upon operation.[23] By stark contrast, even after 504 h of operation, ∼10 nm $Pt/(MnCo)O_x$ nanocouplings are densely distributed on YSZ surface in cell no. 2. Such Pt stabilization on the YSZ surface apparently results from the ALD coating of Pt with CoO_x together. In cell no. 2, the deposited CoO_x layer on YSZ surfaces incorporated the Mn that diffused from the adjacent LSM grains. The incorporation of Mn in the CoO_x ALD layer took place when the cell was heated up to 750 °C, as shown in Figure S8 and Table S2. Thus, Mn cation is readily available in the ALD layer, and the YSZ grain surface is populated with Mn species and possesses certain electrical conductivity.[29] Meanwhile, since $(MnCo)O_x$ is also an active catalyst,[48] ORR easily and first takes place on/ adjacent to the $(MnCo)O_x/YSZ$ interface, and the reduced oxygen ions could be promptly transported away through the ionic conducting YSZ grains. Such ORR and the associated reduced oxygen partial pressure could further induce the reduction of Pt−O and the sequential local reassembly of nano-Pt right at the $(CoMn)O_x/YSZ$ interface. Consequently, the $(CoMn)O_x$ thus serves as an incubating catalyst for stabilizing Pt that is much active for ORR over the prolonged electrochemical operation. Overall, electrochemical operation on the backbone surface promotes the synergetic coupling between two catalysts of Pt and $(MnCo)O_x$ and facilitates the formation of $Pt/(MnCo)O_x$ nanocoupling.

In the meantime, on the LSM backbone, the Pt/Co−Mn−O pairs are also populating along the LSM/LSM surface grain boundaries. Since Pt only reassembles at the ORR active sites with lower oxygen partial pressure, the distribution of Pt grains reveals the existence of effective TPBs at the LSM/LSM surface grain boundaries. In general, the LSM is an excellent electronic conductor and with neglectable intragranular ionic conductivity. The existence of nano-Pt immediately suggests that the Co-doped LSM surface grain boundaries possess ionic conductivity, as schematized in Figure 4e. The present work is fully consistent with the density function calculation[49] and provides the first experimental evidence showing that the grain boundaries from electrically conducting LSM could possess substantial ionic conductivity.

3.4. Nanostructure Origin of Resistance Reduction and the Accelerated ORR. In cell no. 2, the $Pt/(MnCo)O_x$ couplings at the original TPB regions have introduced more active catalyst Pt for accelerated ORR. On the YSZ surface, the spacing of the neighboring $Pt/(MnCo)O_x$ dual-catalysts coupling is ∼10 nm, that is less than where the active TPB could be extended to through polarization.[50] Accordingly, for the YSZ surface that was originally electrochemically inactive, there are high-density newly implanted effective TPBs. On the other hand, due to the engineered percolating network for the electronic conductor LSM in the LSM/YSZ composite electrode, the grain boundaries on the LSM surface are expected to be percolating over the entire cathode surface, thus
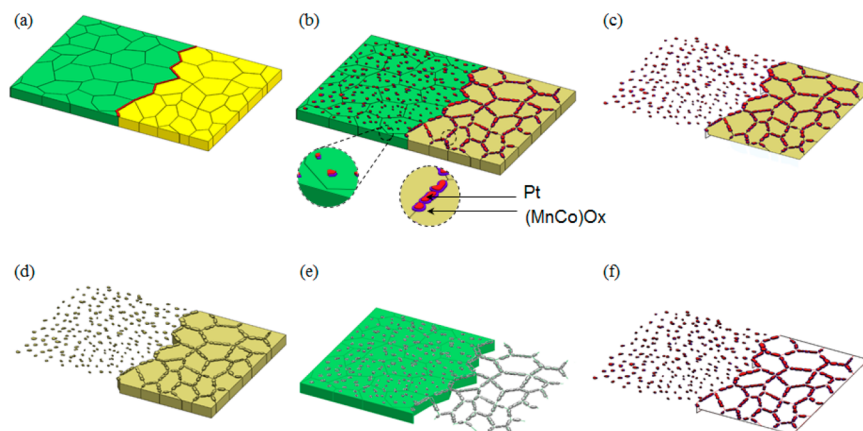
Figure 4. Schematic of the surface architecture of cell no. 1 and cell no. 2. (a) Baseline LSM/YSZ interface and the original TPB. (b) Cell no. 2 with the Pt/Mn−Co−O pair uniformly distributed on YSZ surface and along the LSM/LSM grain boundaries. (c) Distribution of active catalyst for ORR in cell no. 2. (d) Distribution of electronic conductor in cell no. 2. (e) Distribution of ionic conductor and ionic conducting interfaces in cell no. 2. (f) Distribution of effective TPBs in cell no. 2.

adding an active pathway to the oxide ion transport. Therefore, the Pt/(MnCo)O$_x$ couplings at LSM/LSM surface grain boundaries are active sites and effective TPBs contributing to the ORR as well.

Overall, for the baseline cell in which the kinetics of the LSM cathode is surface-controlled, the ORR is restricted to the TPBs. On the other hand, for the ALD-coated cell, active sites extend from original TPBs to YSZ grain surfaces and grain boundaries of Co-doped LSM. Consequently, there is substantial and active involvement of the cathode bulk in the overall electrode reaction, as evidenced by the apparent changes in chemical capacitance[43,44] introduced by ALD coating as shown in Figures S2−S6 and Table S1.

In terms of the catalysts, more active nano-Pt catalyst added to the original TPBs, the newly implanted catalysts and TPBs on the YSZ grain surfaces and the LSM grain surface dramatically accelerate the ORR, promotes the additional oxygen surface diffusion and subsequent dissociative adsorption of oxygen molecules.[39] Such accelerated ORR is well-illustrated with the reduced cell impedance as retrieved by the associated deconvolution spectrum. As shown in Figure 1d, there is a significant reduction of P$_1$ and P$_2$ in the deconvolution spectrum from cell no. 2, in comparison with that of the baseline cell. The further electrochemical operation has little effect on P$_1$, implying Pt/(MnCo)O$_x$ couplings are stable. Special attention needs to be given to the peak P$_2$ in Figure 1d at 40−80 Hz. P$_2$ in cell no. 2 is dramatically lower than that in cell no. 1 at 0 h of operation. Nevertheless, the amplitude of the P$_2$ in cell no. 2 increases and shifts to the lower frequency range with the increase of the operation time. In general, P$_2$ is believed to be associated with the oxygen incorporation, and oxygen ion transport within the cathode, and it strongly depends on the cathode structure and composition.[41] The shift of P$_2$ arcs in cell no. 2 indicates a continuous change in the chemistry of the cathode with the increase of operation. As mentioned previously, the as-deposited ALD consists of the superjacent CoO$_x$ layer, and Co populates on the LSM surface layer. The Co-doped LSM possesses substantial ionic conductivity and thus creates additional pathways for oxygen transport and extends TPB length on the LSM surface. There is also evidence showing that the amount of Co level in La$_{0.8}$Sr$_{0.2}$Mn$_{1−x}$Co$_x$O$_3$ perovskites which results in the maximum oxygen transport is ∼25%.[29] Upon operation, Co from the ALD layer diffuses into the interior of the bulk LSM, but the supply of Co is very limited due to the thinness of the ALD capping layer. The diminishing Co in the surface layer could impact the ionic conductivity of the LSM and result in the P$_2$ increase. However, after 504 h of operations at 750 °C, it is believed that Co concentration in the LSM reached the equilibrium as evidenced by the very little variation of Co concentration between the LSM surface layer and grain interior (Figure 3 and Table 2). Both the Pt/(MnCo)O$_x$ catalytic nanocoupling and enhanced cell performance are expected to prolong upon further electrochemical operations at elevated temperatures.

4. SUMMARY

A coating layer, consisting of dual catalysts of a superjacent 2 nm CoO$_x$ layer and superjacent 3 nm discrete Pt particles, was precisely deposited on the internal surface of an LSM/YSZ composite cathode of a state-of-the-art commercial cell via ALD. The dual-electrocatalyst coating immediately promotes the cell performance with the increase of its peak power

density to ∼300% compared to that of the baseline cell. After 504 h of operation, the ALD-modified cathode retains the high ORR activity, and its peak power density remains ∼200% over that of the baseline cell. Nanostructure analyses reveal that the ultrathin ALD layer has evolved into Pt/(MnCo)O$_x$ nano-couplings driven by the synergetic interaction with the cathode backbone and the sequential ORR activities associated with the two different catalysts. For the first time in the field of high-temperature ceramic cells, this study demonstrates an effective approach of stabilizing the minute amount of nano-Pt catalyst for enhancing the ORR activity at elevated temperatures. Most importantly, for the YSZ surface that was originally electro-chemically inactive, there are high-density newly implanted effective TPBs for accelerated ORR. In addition to the surface of the YSZ and the original TPBs, the Pt/(MnCo)O$_x$ couplings are also densely distributed at the LSM/LSM surface grain boundaries. The present work thus also provides the first experimental evidence showing that the grain boundaries from electrically conducting LSM could possess substantial ionic conductivity.

■ ASSOCIATED CONTENT

Ⓢ Supporting Information

The Supporting Information is available free of charge on the ACS Publications website at DOI: 10.1021/acscatal.9b00811.

> Schematic of the as-deposited ALD layer with dual catalysts, impedance deconvolution and equivalent circuit simulations, TEM images of Pt on the YSZ grain surface, and TEM images and EDS of the ALD layer with manganese incorporation (PDF)

■ AUTHOR INFORMATION

Corresponding Author
*E-mail: xueyansong@mail.wvu.edu.

ORCID Ⓘ
Xueyan Song: 0000-0002-9878-5883

Notes
The authors declare no competing financial interest.

■ ACKNOWLEDGMENTS

■ REFERENCES

(1) Choi, S.; Kucharczyk, C. J.; Liang, Y.; Zhang, X.; Takeuchi, I.; Ji, H.; Haile, S. M. Exceptional Power Density and Stability at Intermediate Temperatures in Protonic Ceramic Fuel Cells. *Nat. Energy* **2018**, *3*, 202−210.

(2) Duan, C.; Kee, R. J.; Zhu, H.; Karakaya, C.; Chen, Y.; Ricote, S.; Jarry, A.; Crumlin, E. J.; Hook, D.; Braun, R.; Sullivan, N. P.; O'Hayre, R. Highly Durable, Coking and Sulfur Tolerant, Fuel-flexible Protonic Ceramic Fuel Cells. *Nature* **2018**, *557*, 217−222.

(3) Duan, C.; Tong, J.; Shang, M.; Nikodemski, S.; Sanders, M.; Ricote, S.; Almansoori, A.; O'Hayre, R. Readily Processed Protonic Ceramic Fuel Cells with High Performance at Low Temperatures. *Science* **2015**, *349*, 1321−1326.

(4) Steele, B. C. H.; Heinzel, A. Materials for Fuel-Cell Technologies. *Nature* **2001**, *414*, 345−352.

(5) Lee, K. T.; Wachsman, E. D. Role of Nanostructures on SOFC Performance at Reduced Temperatures. *MRS Bull.* **2014**, *39*, 783−791.

(6) Ding, D.; Li, X.; Lai, S. Y.; Gerdes, K.; Liu, M. Enhancing SOFC Cathode Performance by Surface Modification through Infiltration. *Energy Environ. Sci.* **2014**, *7*, 552−575.

(7) Li, X.; Blinn, K.; Chen, D.; Liu, M. In Situ and Surface-Enhanced Raman Spectroscopy Study of Electrode Materials in Solid Oxide Fuel Cells. *Electrochem. Energy Rev.* **2018**, *1*, 433−59.

(8) Singhal, S. C. Solid Oxide Fuel Cells for Stationary, Mobile, and Military Applications. *Solid State Ionics* **2002**, *152*, 405−410.

(9) Advanced Research Projects Agency—Energy. https://arpa-e.energy.gov/?q=workshop/fuel-cell-and-heat-engine-hybrid-chp-systems (accessed Aug 27, 2018).

(10) Kendall, K.; Kendall, M. *High-Temperature Solid Oxide Fuel Cells for the 21st Century: Fundamentals, Design and Applications*; Elsevier: London, 2015.

(11) Boaro, M.; Aricò, A. S. *Advances in Medium and High Temperature Solid Oxide Fuel Cell Technology*; Springer: Cham, Switzerland, 2017.

(12) Wachsman, E. D.; Lee, K. T. Lowering the Temperature of Solid Oxide Fuel Cells. *Science* **2011**, *334*, 935−939.

(13) Lee, S.; Miller, N.; Gerdes, K. Long-Term Stability of SOFC Composite Cathode Activated by Electrocatalyst Infiltration. *J. Electrochem. Soc.* **2012**, *159*, F301−F308.

(14) Irvine, J. T. S.; Neagu, D.; Verbraeken, M. C.; Chatzichristodoulou, C.; Graves, C.; Mogensen, M. Evolution of The Electrochemical Interface in High-Temperature Fuel Cells and Electrolysers. *Nat. Energy* **2016**, *1*, 15014.

(15) Vohs, J. M.; Gorte, R. High-Performance SOFC Cathodes Prepared by Infiltration. *Adv. Mater.* **2009**, *21*, 943−956.

(16) Lee, S.; Miller, N.; Abernathy, H.; Gerdes, K.; Manivannan, A. Effect of Sr-doped LaCoO3 and LaZrO3 Infiltration on the Performance of SDC-LSCF Cathode. *J. Electrochem. Soc.* **2011**, *158*, B735−B742.

(17) George, S. M. Atomic Layer Deposition: An Overview. *Chem. Rev.* **2010**, *110*, 111−131.

(18) Miikkulainen, V.; Leskela, M.; Ritala, M.; Puurunen, R. L. Crystallinity of Inorganic Films Grown by Atomic Layer Deposition: Overview and General Trends. *J. Appl. Phys.* **2013**, *113*, 021301.

(19) Chao, C.-C.; Motoyama, M.; Prinz, F. B. Nanostructured Platinum Catalysts by Atomic-Layer Deposition for Solid-Oxide Fuel Cells. *Adv. Energy Mater.* **2012**, *2*, 651−654.

(20) Jiang, X.; Gur, T. M.; Prinz, F. B.; Bent, S. F. Atomic Layer Deposition (ALD) Co-Deposited Pt-Ru Binary and Pt Skin Catalysts for Concentrated Methanol Oxidation. *Chem. Mater.* **2010**, *22*, 3024−3032.

(21) O'Neill, B. J.; Jackson, D. H.; Lee, J.; Canlas, C.; Stair, P. C.; Marshall, C. L.; Elam, J. W.; Kuech, T. F.; Dumesic, J. A.; Huber, G. W. Catalyst Design with Atomic Layer Deposition. *ACS Catal.* **2015**, *5*, 1804−1825.

(22) Choi, H. J.; Bae, K.; Grieshammer, S.; Han, G. D.; Park, S. W.; Kim, J. W.; Jang, D. Y.; Koo, J.; Son, J. W.; Martin, M.; Shim, J.-H. Surface Tuning of Solid Oxide Fuel Cell Cathode by Atomic Layer Deposition. *Adv. Energy Mater.* **2018**, *8*, 1802506.

(23) Chen, Y.; Gerdes, K.; Song, X. Nanoionics and Nanocatalysts: Conformal Mesoporous Surface Scaffold for Cathode of Solid Oxide Fuel Cells. *Sci. Rep.* **2016**, *6*, 32997.

(24) Tian, N.; Lu, B.-A.; Yang, X.-D.; Huang, R.; Jiang, Y.-X.; Zhou, Z.-Y.; Sun, S.-G. Rational Design and Synthesis of Low-Temperature Fuel Cell Electrocatalysts. *Electrochem. Energy Rev.* **2018**, *1*, 54−83.

(25) Debe, M. K. Electrocatalyst Approaches and Challenges for Automotive Fuel Cells. *Nature* **2012**, *486*, 43−51.

(26) Chen, D.; Huang, C.; Ran, R.; Park, H. J.; Kwak, C.; Shao, Z. New Ba0.5Sr0.5Co0.8Fe0.2O3−δ+Co3O4 Composite Electrode for IT-SOFCs with Improved Electrical Conductivity and Catalytic Activity. *Electrochem. Commun.* **2011**, *13*, 197−199.

(27) Zhang, Z.; Wang, J.; Chen, Y.; Tan, S.; Shao, Z.; Chen, D. In Situ Formation of A 3D Core-Shell and Triple-Conducting Oxygen Reduction Reaction Electrode for Proton-Conducting SOFCs. *J. Power Sources* **2018**, *385*, 76−83.

(28) Chen, Y.; Hinerman, A.; Liang, L.; Gerdes, K.; Navia, S. P.; Prucz, J.; Song, X. Conformal Coating of Cobalt Oxide on Solid Oxide Fuel Cell Cathode and Resultant Continuously Increased Oxygen Reduction Reaction Kinetics Upon Operation. *J. Power Sources* **2018**, *405*, 45−50.

(29) Bai, Y.; Liu, M.; Ding, D.; Blinn, K.; Qin, W.; Liu, J.; Liu, M. Electrical and Electrocatalytic Properties of a La0.8Sr0.2Co0.17Mn0.83O3-δ Cathode for Intermediate-Temperature Solid Oxide Fuel Cells. *J. Power Sources* **2012**, *205*, 80−85.

(30) Shimada, H.; Yamaguchi, T.; Sumi, H.; Nomura, K.; Yamaguchi, Y.; Fujishiro, Y. Extremely Fine Structured Cathode For Solid Oxide Fuel Cells Using Sr-Doped LaMnO3 and Y2O3-Stabilized ZrO2 Nano-Composite Powder Synthesized by Spray Pyrolysis. *J. Power Sources* **2017**, *341*, 280−284.

(31) Imanishi, N.; Ohno, R.; Murata, K.; Hirano, A.; Takeda, Y.; Yamamoto, O.; Yamahara, K. LSM-YSZ Cathode with Infiltrated Cobalt Oxide and Cerium Oxide Nanoparticles. *Fuel Cells* **2009**, *9*, 215−221.

(32) Wang, W. G.; Liu, Y.-L.; Barfod, R.; Schougaard, S. B.; Gordes, P.; Ramousse, S.; Hendriksen, P. Y.; Mogensen, M. Nanostructured Lanthanum Manganate Composite Cathode. *Electrochem. Solid-State Lett.* **2005**, *8*, A619−A621.

(33) Wilson, J. R.; Barnett, S. A. Solid Oxide Fuel Cell Ni−YSZ Anodes: Effect of Composition on Microstructure and Performance. *Electrochem. Solid-State Lett.* **2008**, *11*, B181−B185.

(34) Liu, J.; Barnett, S. A. Operation of Anode-Supported Solid Oxide Fuel Cells on Methane and Natural Gas. *Solid State Ionics* **2003**, *158*, 11−16.

(35) Lee, J. G.; Park, M.-G.; Ryu, K. H.; Song, R. H.; Park, S. J.; Min, S. H.; Hyun, S.-H.; Kim, C. S.; Shin, D. R.; Shul, Y. G. Performance Improvement of Ni-YSZ-Based Solid Oxide Fuel Cell with the Anode Functional Layer Synthesized by Co-Precipitation Method. *ECS Trans.* **2013**, *57*, 2947−2952.

(36) Ma, Q.; Ma, J.; Zhou, S.; Yan, R.; Gao, J.; Meng, G. A High-Performance Ammonia-Fueled SOFC Based on a YSZ Thin-Film Electrolyte. *J. Power Sources* **2007**, *164*, 86−89.

(37) Storjohann, D.; Daggett, J.; Sullivan, N. P.; Zhu, H.; Kee, R. J.; Menzer, S.; Beeaff, D. Fabrication and Evaluation of Solid-Oxide Fuel Cell Anodes Employing Reaction-Sintered Yttria-Stabilized Zirconia. *J. Power Sources* **2009**, *193*, 706−712.

(38) Sonn, V.; Leonide, A.; Ivers-Tiffée, E. Combined Deconvolution and CNLS Fitting Approach Applied on the Impedance Response of Technical Ni/8YSZ Cermet Electrodes. *J. Electrochem. Soc.* **2008**, *155*, B675−B679.

(39) Liu, B.; Muroyama, H.; Matsui, T.; Tomida, K.; Kabata, T.; Eguchi, K. Analysis of Impedance Spectra for Segmented-In-Series Tubular Solid Oxide Fuel Cells. *J. Electrochem. Soc.* **2010**, *157*, B1858−B1864.

(40) Barfod, R.; Mogensen, M.; Klemenso, T.; Hagen, A.; Liu, Y.-L.; Vang Hendriksen, P. Detailed Characterization of Anode-Supported SOFCs by Impedance Spectroscopy. *J. Electrochem. Soc.* **2007**, *154*, B371−B378.

(41) Leonide, A.; Ruger, B.; Weber, A.; Meulenberg, W. A.; Ivers-Tiffee, E. Impedance Study of Alternative (La,Sr)FeO3-δ and (La,Sr)(Co,Fe)O3-δ MIEC Cathode Compositions. *J. Electrochem. Soc.* **2010**, *157*, B234−B239.

(42) Finklea, H.; Chen, X.; Gerdes, K.; Pakalapati, S.; Celik, I. Analysis of SOFCs Using Reference Electrodes. *J. Electrochem. Soc.* **2013**, *160*, F1055−F1066.

(43) Kawada, T.; Suzuki, J.; Sase, M.; Kaimai, A.; Yashiro, K.; Nigara, Y.; Mizusaki, J.; Kawamura, K.; Yugami, H. Determination of Oxygen Vacancy Concentration in a Thin Film of La0.6Sr0.4CoO3-δ by an Electrochemical Method. *J. Electrochem. Soc.* **2002**, *149*, E252−E259.

(44) Baumann, F. S.; Fleig, J.; Habermeier, H.-U.; Maier, J. Impedance Spectroscopic Study on Well-Defined (La,Sr)(Co,Fe)O3-δ Model Electrodes. *Solid State Ionics* **2006**, *177*, 1071−1081.

(45) Shin, S. M.; Yoon, B. Y.; Kim, J. H.; Bae, J. M. Performance Improvement by Metal Deposition at the Cathode Active Site in Solid Oxide Fuel Cells. *Int. J. Hydrogen Energy* **2013**, *38*, 8954−8964.

(46) Xiong, Y.; Yamaji, K.; Kishimoto, H.; Brito, M. E.; Horita, T.; Yokokawa, H. Deposition of Platinum Particles at LSM/ScSZ/Air Three-Phase Boundaries Using a Platinum Current Collector. *Electrochem. Solid-State Lett.* **2009**, *12*, B31−B33.

(47) Backhaus-Ricoult, M. Interface Chemistry in LSM-YSZ Composite SOFC Cathodes. *Solid State Ionics* **2006**, *177*, 2195−200.

(48) Liu, H.; Zhu, X.; Cheng, M.; Cong, Y.; Yang, W. Novel $Mn_{1.5}Co_{1.5}O_4$ Spinel Cathodes for Intermediate Temperature Solid Oxide Fuel Cells. *Chem. Commun.* **2011**, *47*, 2378−2380.

(49) Polfus, J. M.; Yildiz, B.; Tuller, H. L. Origin of Fast Oxide Ion Diffusion along Grain Boundaries in Sr-Doped $LaMnO_3$. *Phys. Chem. Chem. Phys.* **2018**, *20*, 19142−19150.

(50) Adler, S. B. Factors Governing Oxygen Reduction in Solid Oxide Fuel Cell Cathodes. *Chem. Rev.* **2004**, *104*, 4791−4843.